Compressive failure of woven fabric reinforced thermoplastic composites with an open-hole: An experimental and numerical study

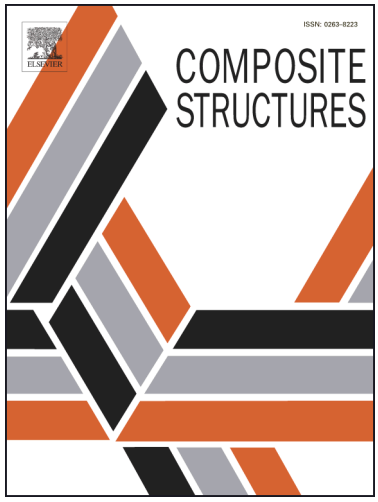

Compressive failure of woven fabric reinforced thermoplastic composites with an open-hole: an experimental and numerical study

Haibao Liu, Shipeng Li, Wei Tan, Jun Liu, Hui Chai, Bamber R.K. Blackman, John P. Dear

PII: S0263-8223(18)33710-3
DOI: https://doi.org/10.1016/j.compstruct.2019.01.070
Reference: COST 10587

To appear in: *Composite Structures*

Received Date: 24 October 2018
Revised Date: 28 December 2018
Accepted Date: 14 January 2019

Please cite this article as: Liu, H., Li, S., Tan, W., Liu, J., Chai, H., Blackman, B.R.K., Dear, J.P., Compressive failure of woven fabric reinforced thermoplastic composites with an open-hole: an experimental and numerical study, *Composite Structures* (2019), doi: https://doi.org/10.1016/j.compstruct.2019.01.070

Compressive failure of woven fabric reinforced thermoplastic composites with an open-hole: an experimental and numerical study

Haibao Liu[a, *], Shipeng Li [b], Wei Tan [c], Jun Liu [a], Hui Chai [d],

Bamber R.K. Blackman [a], John P. Dear [a, *]

[a] *Department of Mechanical Engineering, Imperial College London, South Kensington Campus, London SW7 2AZ, UK*

[b] *Key Laboratory of Mechanism Theory and Equipment Design of Ministry of Education, Tianjin University, Tianjin 300350, People's Republic of China*

[c] *Department of Engineering, University of Cambridge, Trumpington Street, Cambridge, CB2 1PZ, UK*

[d] *The First Aircraft Institute, No.1 East Renmin Road, Yanliang District, Xi'an, Shaanxi 710089, People's Republic of China*

* Corresponding Authors: Dr Haibao Liu and Professor John P. Dear

ABSTRACT

This research presents a detailed experimental and numerical study on the compressive failure of woven fabric reinforced thermoplastic composites, with an open-hole and with a pinned open-hole. The experimental evaluations are performed on the composite specimens using the Combined Loading Compression (CLC) evaluation method. Experimental results, including load response and damage morphology, are obtained and analysed. A meso-scale damage model is developed, based on Continuum-Damage-Mechanics (CDM), for predicting damage in woven fabric reinforced composites. The developed model, which can capture fibre fracture and matrix cracking, as well as the nonlinear response within the woven composite materials, is employed to conduct virtual Combined Loading Compression (CLC) tests. Numerical simulation results are compared with the extracted experimental results for model validation. Good correlation is achieved between experimental and computational results for both the open-hole and the pinned open-hole, with a two-stage failure process being observed for the pinned open-hole.

Key words: *Woven composites, Combined Loading Compression (CLC), Damage mechanism, Finite Element Analysis (FEA)*

1. Introduction

Over the past twenty years, composite materials have found much application in the transport industries, particularly in the aeronautical sector. However, due to their complex intrinsic properties, the damage mechanisms of composite structures under some loading conditions, e.g., the compressive loading, is still not clear. A better understanding of the loading behaviour and onset of damage in composite materials is required for the design and maintenance of composite structures. Although the loading response of composite structures and associated failure can be obtained from experimental evaluations [1–5], this can consume considerable time and is costly. A material evaluation and design methodology which is low-cost, with high confidence, is required by the transport industries. With this in mind, much research has been devoted to the development of high-fidelity damage models, which can significantly reduce the design and maintenance cost of composite structures.

A number of computational models have been developed by researchers to predict damage in unidirectional carbon-fibre reinforced composites [6–10]. An approach, which is based on contact constraint introduced by a penalty function method, was proposed by Zhang et al. [11] to predict the damage initiation and damage propagation in composite laminates. In their model, the potential delamination and matrix cracking areas are considered as a cohesive zone. A scalar damage variable was introduced to indicate the degradation of the interfacial stiffness. The stress-based and fracture-mechanics-based failure criteria were combined to derive the damage evolution law. The damage model was implemented as a user subroutine in Abaqus and validated using the experimental results obtained from impact tests. Tan et al. [12] used a three-dimensional (3D) composite damage model, which accounts for both interlaminar and intralaminar failure, to predict the crush behaviour of unidirectional carbon-fibre reinforced composite laminates. The interlaminar damage model was created using the in-built cohesive behaviour in Abaqus. The failure mechanisms of fibre and matrix, subjected to 3D stress state, were considered in the intralaminar damage model, which was implemented as a user subroutine in Abaqus/Explicit. Good agreement was achieved between experimental observations and numerical simulation.

Experimental investigations have shown that woven fabric reinforced composite structures exhibit a higher interlaminar strength and damage tolerance than unidirectional composite structures, which has motivated the increasing application of woven composites [13]. The increasing utilisation of woven composites requires the development of a corresponding computational model.

Compared to the number of reported computational models for unidirectional composites, fewer woven damage models have been reported. Iannucci and Willows [14,15] proposed an energy-based damage model, which was implemented into the explicit dynamic DYNA3D code for plane stress shell elements, for capturing the response of woven carbon-fibre reinforced composites. An interface modelling strategy was also presented to predict the delamination between composite plies due to impact loading. A series of physical impact tests at different energy levels were performed for the model validation. A detailed parameter study was conducted using the validated model to discuss the effects of the magnitude of the intralaminar energy release rate on the damage propagation in woven carbon composites. Donadon et al. [16] presented an analytical model for predicting the elastic behaviour of plain-weave fabric composites. In their research, the effective material properties were derived based on Classical Laminate Theory (CLT). The theoretical predictions of this model were compared to the results from experiment and other predictive models reported by other researchers. A good correlation was obtained between theoretical and experimental results for the prediction of in-plane properties.

In the present research, Combined Loading Compression (CLC) tests have been performed on the open-hole composite samples, with and without a pin, through the hole. A physically-based damage model has been developed for predicting damage in woven fabric reinforced composite structures. An in-house intralaminar damage model, which includes fibre/matrix-dominated damage initiation, energy-based damage progression and nonlinear properties, was developed based on the composite damage model proposed by Falzon et al. [17–22]. The in-built cohesive-surface behaviour in Abaqus/explicit was used to capture the interlaminar failure (delamination). The combination of interlaminar and intralaminar damage models enables the development of a damage model to capture different composite failure modes, such as fibre fracture and matrix cracking as well as delamination. The simulation of the compression events was conducted in Abaqus 2017 using the developed

computational model. The numerical results, including load versus time histories and damage morphology were compared with the corresponding experimental results.

2. Woven damage model

2.1 Theoretical foundations

2.1.1 Failure modes

The failure modes, including delamination, fibre damage and matrix damage [21,23], which may occur in a woven composite ply are shown in Fig. 1a. In the woven composite damage model, damage may be initiated on surfaces W1, W2 and W3, according to the Northwestern University (NU) criteria for woven composites [24]. Damage may evolve and energy may dissipate on these surfaces, which are perpendicular to global directions 1, 2 and 3 respectively, as shown in Fig 1b.

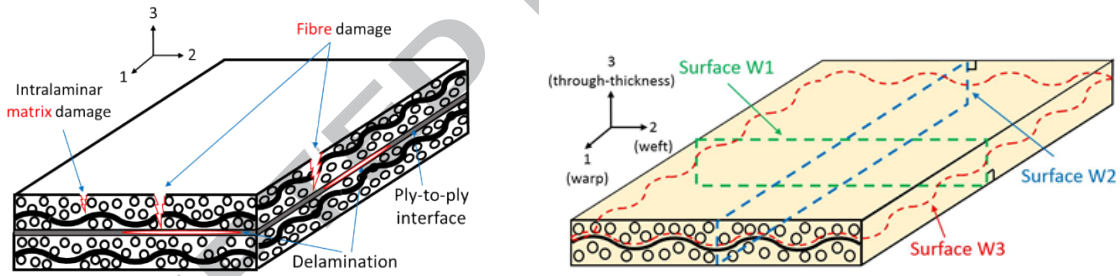

(a) (b)

Fig. 1. Failure of woven composite ply [17]: (a) Failure modes and (b) Associated fracture planes in the woven composite damage model.

2.1.2 Continuum Damage Mechanics

The basic concept in Continuum Damage Mechanics (CDM) [25] is that microscopic cracks and voids form within the material under loading [26] before the onset of macroscopic fracture as shown in Fig. 2a, where the black dots represent the micro-cracking.

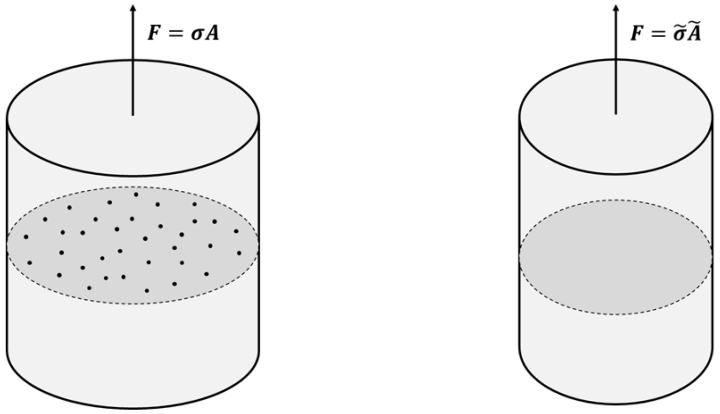

Fig. 2. CDM model: (a) Cross-sectional area, A, with micro-cracking and (b) the reduced effective load bearing area, Ã [21].

In Fig. 2a, the micro-cracking in the original material under damage-inducing load, F, leads to a reduction in the effective load bearing area, from the cross-sectional area, A, of the original (damaged) specimen to the reduced effective load bearing area, $\tilde{A}$, represented by a fictitious state of the material shown in Figure 2b. The reduction of the load bearing area (from A to $\tilde{A}$) may be quantified by a damage parameter, d, given by:

$$d = 1 - \frac{\tilde{A}}{A} \quad . \tag{1}$$

This reduction in load bearing area leads to a corresponding reduction in transmitted stress, σ, in the damaged material. The transmitted stress, σ, was related to an 'effective' stress, $\tilde{\sigma}$, in the 'fictitious' undamaged configuration, given by:

$$\sigma = (1 - d)\tilde{\sigma} \quad . \tag{2}$$

Based on the principle of strain equivalence, the strain in the damaged material (Fig. 2a) and fictitious material (Fig. 2b) are assumed to be equal:

$$\varepsilon = \frac{\sigma}{E} = \frac{(1-d)\tilde{\sigma}}{(1-d)\tilde{E}} = \tilde{\varepsilon} \quad . \tag{3}$$

Using the constitutive relations, $\sigma = E\varepsilon$ and $\tilde{\sigma} = \tilde{E}\tilde{\varepsilon}$, where E is the modulus of the damaged material and $\tilde{E}$ is the modulus of the fictitious (undamaged/pristine) material, it may be easily shown that:

$$E = (1-d)\tilde{E} \quad . \tag{4}$$

2.1.3 Global constitutive law

The effective stresses are defined as stresses transmitted across the intact part of the cross-section in a Representative Volume Element (RVE). The components of the effective stress tensor, $\tilde{\boldsymbol{\sigma}}$, and strain tensor, $\boldsymbol{\varepsilon}$, can be linked by the stiffness matrix, $\boldsymbol{C}$, given by:

$$\tilde{\boldsymbol{\sigma}} = \boldsymbol{C}:\boldsymbol{\varepsilon} \quad , \tag{5}$$

where

$$\mathbf{C} = \begin{pmatrix} E_1\frac{1-\nu_{23}\nu_{32}}{\delta} & E_1\frac{\nu_{21}+\nu_{31}\nu_{23}}{\delta} & E_1\frac{\nu_{31}+\nu_{21}\nu_{32}}{\delta} & 0 & 0 & 0 \\ E_2\frac{\nu_{12}+\nu_{32}\nu_{13}}{\delta} & E_2\frac{1-\nu_{13}\nu_{31}}{\delta} & E_2\frac{\nu_{32}+\nu_{12}\nu_{31}}{\delta} & 0 & 0 & 0 \\ E_3\frac{\nu_{13}+\nu_{12}\nu_{23}}{\delta} & E_3\frac{\nu_{23}+\nu_{21}\nu_{13}}{\delta} & E_3\frac{1-\nu_{12}\nu_{21}}{\delta} & 0 & 0 & 0 \\ 0 & 0 & 0 & 2G_{12} & 0 & 0 \\ 0 & 0 & 0 & 0 & 2G_{23} & 0 \\ 0 & 0 & 0 & 0 & 0 & 2G_{13} \end{pmatrix} ,$$

$$\delta = 1 - \nu_{12}\nu_{21} - \nu_{23}\nu_{32} - \nu_{13}\nu_{31} - 2\nu_{21}\nu_{32}\nu_{13} \quad ,$$

$$\nu_{ij} = \frac{E_i}{E_j}\nu_{ji} \quad .$$

After damage initiation, both the moduli and Poisson's ratios are degraded:

$$\frac{\nu_{ij,d}}{E_{ii,\,d}} = \frac{\nu_{ij}(1-d_{ii})}{E_{ii}(1-d_{ii})} = \frac{\nu_{ji}(1-d_{jj})}{E_{jj}(1-d_{jj})} = \frac{\nu_{ji,d}}{E_{jj,\,d}}, i,j = 1,2,3\ i \neq j \quad . \tag{6}$$

2.2 Damage model for fibre failure

2.2.1 Fibre-dominated damage initiation

In a woven composite ply, the warp and weft material responses are dominated by fibres, which are assumed to be elastic responses. A strain-based damage criterion [27,28] was employed to govern the damage initiation in both warp and weft directions:

$$F_{11/22}^{T} = \left(\frac{\varepsilon_{11/22}}{\varepsilon_{11/22}^{OT}}\right)^2 , \tag{7}$$

$$F_{11/22}^{C} = \left(\frac{\varepsilon_{11/22}}{\varepsilon_{11/22}^{OC}}\right)^2 , \tag{8}$$

where $F_{11/22}^{T}$ and $F_{11/22}^{C}$ are the failure indices for tensile damage and compressive damage in the warp/weft direction respectively. The strain, $\varepsilon_{11/22}$, is the current value in warp/weft direction respectively. The strains in the fibre-dominated directions, $\varepsilon_{11/22}^{OT}$ and $\varepsilon_{11/22}^{OC}$, correspond to tensile damage and compressive damage initiation in the warp/weft direction respectively.

2.2.2 Damage evolution for fibre fracture

Damage variables, $d_{11/22}^{T}$ and $d_{11/22}^{C}$, were defined to evaluate the fibre damage evolution in warp/weft direction, due to tensile and compressive loading respectively in the woven composite model. The damage parameters for the fibre-dominated failure are given by:

$$d_{11/22}^{T} = \frac{\varepsilon_{11/22}^{FT}}{\varepsilon_{11/22}^{FT/FC} - \varepsilon_{11/22}^{OT}}\left(1 - \frac{\varepsilon_{11/22}^{OT}}{\varepsilon_{11/22}^{T}}\right) , \tag{9}$$

$$d_{11/22}^{C} = \frac{\varepsilon_{11/22}^{FC}}{\varepsilon_{11/22}^{FC} - \varepsilon_{11/22}^{OC}}\left(1 - \frac{\varepsilon_{11/22}^{OC}}{\varepsilon_{11/22}^{C}}\right) ,$$

where $\varepsilon_{11/22}^{OT}$ and $\varepsilon_{11/22}^{OC}$ are the strains at fibre-dominated tensile and compressive damage initiation in the warp/weft direction, respectively. The current strains, $\varepsilon_{11/22}^{T}$ and $\varepsilon_{11/22}^{C}$, are due to fibre-dominated

tensile and fibre-dominated compressive loading in the warp/weft direction. The final failure strains, $\varepsilon_{11/22}^{FT}$ and $\varepsilon_{11/22}^{FC}$, refer to the fibre-dominated tensile and compressive failure, given by:

$$\varepsilon_{11/22}^{FT} = \frac{2G_{Ic}|_{ft}}{X^T l_{fib}} \quad , \tag{10}$$

$$\varepsilon_{11/22}^{FC} = \frac{2G_{Ic}|_{fc}}{X^C l_{fib}} \quad , \tag{11}$$

where $G_{Ic}|_{ft}$ and $G_{Ic}|_{fc}$ are the intralaminar fibre-dominated tensile and compressive fracture toughness, respectively. X^T and X^C are the tensile and compressive strengths in fibre direction, respectively. The characteristic length, l_{fib}, in the warp and weft direction is the ratio of the element volume, V, and the area of corresponding representative fracture surface, A_{fib}, as reported in [22].

2.3 Damage model for matrix cracking

2.3.1 Matrix-dominated damage initiation

In this research, the Northwestern University (NU) criterion for woven composites [24] was employed to capture the matrix damage initiation in a woven composite ply. This stress-based damage initiation criterion, which considered the 3D load state [29], is given below:

Tension dominated failure:

$$F_{mat}^{T} = \left(\frac{\sigma_{33}}{\sigma_{33}^{OT}}\right)^2 + \left(\frac{\tau_{13}}{\tau_{13}^{O}}\right)^2 + \left(\frac{\tau_{23}}{\tau_{23}^{O}}\right)^2, \sigma_{33} > 0 \quad , \tag{12}$$

Compression dominated failure:

$$F_{mat}^{C} = \left(\frac{\sigma_{33}}{\sigma_{33}^{OC}}\right)^2 + \left(\frac{E_{33}}{G_{13}}\right)^2\left(\frac{\tau_{13}}{\sigma_{33}^{OC}}\right)^2 + \left(\frac{E_{33}}{G_{23}}\right)^2\left(\frac{\tau_{23}}{\sigma_{33}^{OC}}\right)^2, \sigma_{33} \leq 0 \text{ and } |\sigma_{33}| \geq |\tau_{13/23}| \quad , \tag{13}$$

Shear dominated failure:

$$F_{mat}^{s1} = \left(\frac{\tau_{13}}{\tau_{13}^{O}}\right)^2 + \left(\frac{\tau_{12}}{\tau_{12}^{O}}\right)^2 \quad , \tag{14}$$

$$F_{mat}^{s2} = \left(\frac{\tau_{12}}{\tau_{12}^{O}}\right)^2 + \left(\frac{\tau_{23}}{\tau_{23}^{O}}\right)^2 \quad , \tag{15}$$

$$F_{mat}^{s3} = \left(\frac{\tau_{13}}{\tau_{13}^{O}}\right)^2 + \left(\frac{\tau_{23}}{\tau_{23}^{O}}\right)^2 + 2\frac{G_{13}\sigma_{33}}{E_{33}\tau_{13}^{O}}, \sigma_{33} \leq 0 \text{ and } |\sigma_{33}| \leq |\tau_{13/23}| \quad , \tag{16}$$

where $F_{\mathrm{mat}}^{T/C}$ are the failure indices for matrix-dominated tensile/compressive damage on surface W3. F_{mat}^{s1} and F_{mat}^{s2} are the failure indices for inter-fibre shear damage on surfaces W1 and W2, respectively, and F_{mat}^{s3} is the matrix-dominated shear failure on surface W3. $\sigma_{ii}\ (i = 3)$ and τ_{ij} $(i, j = 1, 2, 3)$ are the stresses acting on surfaces W1, W2 and W3. The stress value, $\sigma_{33}^{OT/OC}$, represents the matrix tensile/compressive strength, and $\tau_{ij}^{O}\ (i, j = 1, 2, 3, i \neq j)$ represents the matrix shear strength of a woven composite ply.

2.3.2 Damage evolution for matrix cracking

The stresses, $\sigma_{ii}\ (i = 3)$ and $\tau_{ij}\ (i, j = 1, 2, 3)$, acting on the surfaces W1, W2 and W3, were combined on the corresponding fracture surfaces. The combined stresses, $\sigma_i\ (i = 1, 2, 3)$, are given by,

$$\sigma_1 = \sqrt{(\tau_{12})^2 + (\tau_{13})^2} \quad , \tag{17}$$

$$\sigma_2 = \sqrt{(\tau_{12})^2 + (\tau_{23})^2} \quad , \tag{18}$$

$$\sigma_3 = \sqrt{(\sigma_{33})^2 + (\tau_{13})^2 + (\tau_{23})^2} \quad . \tag{19}$$

The combined strains, $\varepsilon_i (i = 1, 2, 3)$, which correspond to the combined stresses, $\sigma_i (i = 1, 2, 3)$, acting on the surfaces W1, W2 and W3, were defined as the sum of the l^2-norms of corresponding elastic and inelastic strain vectors, $\varepsilon_i = \varepsilon_{i,el} + \varepsilon_{i,in}\ (i = 1, 2, 3)$, where:

$$\varepsilon_{1,el} = \sqrt{\left(\gamma_{12}^{el}\right)^2 + \left(\gamma_{13}^{el}\right)^2} \quad , \tag{20}$$

$$\varepsilon_{1,in} = \sqrt{\left(\gamma_{12}^{in}\right)^2 + \left(\gamma_{13}^{in}\right)^2} \quad , \tag{21}$$

$$\varepsilon_{2,el} = \sqrt{\left(\gamma_{12}^{el}\right)^2 + \left(\gamma_{23}^{el}\right)^2} \quad , \tag{22}$$

$$\varepsilon_{2,in} = \sqrt{\left(\gamma_{12}^{in}\right)^2 + \left(\gamma_{23}^{in}\right)^2} \quad , \tag{23}$$

$$\varepsilon_{3,el} = \sqrt{\left(\varepsilon_{33}\right)^2 + \left(\gamma_{13}^{el}\right)^2 + \left(\gamma_{23}^{el}\right)^2} \quad , \tag{24}$$

$$\varepsilon_{3,in} = \sqrt{\left(\gamma_{13}^{in}\right)^2 + \left(\gamma_{23}^{in}\right)^2} \quad . \tag{25}$$

In the matrix-dominated failure mode, the monotonous variables, d_i $(i = 1, 2, 3)$, were defined to indicate the evolution of matrix damage due to a combination of tension/compression and shear loading. d_i $(i = 1, 2, 3)$ is a function of the combined strain, $\varepsilon_i (i = 1, 2, 3)$, given by:

$$d_i = \frac{\varepsilon_i^f - \varepsilon_{i,in}^o}{\varepsilon_i^f - \varepsilon_i^o}\left(1 - \frac{\varepsilon_i^o - \varepsilon_{i,in}^o}{\varepsilon_i - \varepsilon_{i,in}^o}\right) \quad , \tag{26}$$

where ε_i^o $(i = 1, 2, 3)$ and $\varepsilon_{i,in}^o$ $(i = 1, 2, 3)$ are the l^2 – norm of the total strains, ε_{ij}^o, ε_{ij}^o and ε_{ij}^o, ($i,j = 1, 2, 3)$, and inelastic strains ($\varepsilon_{ij,in}^o$ and $\varepsilon_{ij,in}^o$, $i,j = 1, 2, 3)$ at damage initiation, respectively. ε_i^f ($i = 1, 2, 3)$ is the l^2– norm of the final strains, ε_{ij}^f $(i,j = 1, 2, 3)$, given by:

$$\varepsilon_i^f = \frac{2G_i^C}{\sigma_i^o \times l_{mat}} \quad , \tag{27}$$

where G_i^C $(i = 1, 2, 3)$ is the critical Mixed-Mode strain energy release rate, and σ_i^0 $(i = 1, 2, 3)$ is l^2-norms of acting stresses at damage initiation. l_{mat}, the characteristic length in the through-thickness direction, equals the ratio of the element volume, V, and the area of the corresponding representative fracture surface, A_{mat}, as reported in [22]. The critical mixed-mode strain energy release rate, G_i^C $(i = 1, 2, 3)$, is given by:

$$G_1^C = G_{IIc}|_{ms}\left(\frac{\gamma_{12}^o}{\sigma_1^o}\right)^2 + G_{IIc}|_{ms}\left(\frac{\gamma_{13}^o}{\sigma_1^o}\right)^2 \quad , \tag{28}$$

$$G_2^C = G_{IIc}|_{ms}\left(\frac{\gamma_{12}^o}{\sigma_2^O}\right)^2 + G_{IIc}|_{ms}\left(\frac{\gamma_{23}^o}{\sigma_2^O}\right)^2 \quad , \tag{29}$$

$$G_3^C = G_{Ic}|_{mt/mc}\left(\frac{\sigma_{33}^o}{\sigma^{OT/OC}_3}\right)^2 + G_{IIc}|_{ms}\left(\frac{\gamma_{13}^o}{\sigma_3^O}\right)^2 + G_{IIc}|_{ms}\left(\frac{\gamma_{23}^o}{\sigma_3^O}\right)^2 \quad , \tag{30}$$

where $G_{Ic}|_{mt/mc}$ and $G_{IIc}|_{ms}$ is the intralaminar fracture toughness associated with matrix-dominated tensile/compressive and shear failure. $\sigma_i^O\ (i = 1, 2, 3)$ is the l^2 – norm of stresses at damage initiation, $\sigma_{ii}^o\ (i = 3)$ and $\gamma_{ij}^o\ (i,j = 1, 2, 3)$, acting on surfaces W1, W2 and W3.

2.4 Nonlinear shear response

The shear response, required by the damage model, was obtained from standard V-notched Rail Shear (VRS) tests and expressed as:

$$\tau(\gamma_{ij}) = c_1\left[sign\ (\gamma_{ij})exp(c_2 sign\ (\gamma_{ij})\gamma_{ij}) - sign\ (\gamma_{ij})exp(c_3 sign\ (\gamma_{ij})\gamma_{ij})\right] \quad , \tag{31}$$

where $c_i(i = 1, 2, 3)$ are coefficients, and $\gamma_{ij}(i,j = n, s, t, i \neq j)$ are the shear strains [30]. Prior to damage initiation, shear loading and unloading occurs along gradients defined by the initial shear moduli G_{ij}. The values of $c_i(i = 1, 2, 3)$ obtained from VRS tests are presented in Table 2.

2.5 Damage model for delamination

In the proposed damage model, the delamination in woven composite structures was captured using the built-in surface-based cohesive behaviour in Abaqus/Explicit. The interlaminar failure initiation is governed by a quadratic stress criterion, which is given by:

$$\left(\frac{\langle\sigma_n\rangle}{\sigma_n^0}\right)^2 + \left(\frac{\tau_s}{\tau_s^0}\right)^2 + \left(\frac{\tau_t}{\tau_t^0}\right)^2 \leq 1 \quad , \tag{32}$$

where σ_n and τ_s (τ_t) are the current normal and in-plane shear stresses respectively. σ_n^0 and τ_s^0 (τ_t^0) are the respective maximum stresses in each direction. For the evolution of interlaminar damage, the energy-based Benzeggagh–Kenane (B-K) propagation criterion [31] was used to propagate the delamination between composite plies, given by:

$$G_c = G_{Ic} + (G_{IIc} - G_{Ic})B^{\eta} \quad , \tag{33}$$

where G_c is the current total Mixed-Mode strain energy release rate, and η is the Mixed-mode interaction exponent determined using the test method described in the ASTM D6671/D6671M-03 testing standard [32]. Parameter B is the local mixed-mode ratio, given by:

$$B = G_{II}/G_I + G_{II} \quad , \tag{34}$$

Parameters G_I and G_{II} are the current Mode I and Model II strain energy release rates, respectively, which can be obtained by multiplying the stresses, σ_n and τ_s (τ_t) shown in Eq. (32), with their conjugate separations δ_i $(i = n, s, t)$, given by [33]:

$$G_I = \langle \sigma_n \rangle \times \delta_n \quad , \tag{35}$$

$$G_{II} = \tau_s \times \delta_s + \tau_t \times \delta_t \quad , \tag{36}$$

In this way, the proportion of current Model II strain energy release rate (G_{II}) in the current total strain energy release rate ($G_I + G_{II}$), which is denoted as the local mixed-mode ratio (B) in Eqs. (33) and (34), can be obtained. Consequently, the current total mixed-mode strain energy release rate, G_c, can be determined based on the measured G_{Ic}, G_{IIc} and η as well as the calculated B. It can be found that the acquisition of current stresses, σ_n and τ_s (τ_t) in Eq. (32), are relevant to the developed intralaminar damage model, illustrated in Eqs. (7)-(31).

2.6 Stress degradation

The degraded stress vector, $\boldsymbol{\sigma}_{123}$, on the surfaces W1, W2 and W3 may then be expressed as:

$$\boldsymbol{\sigma}_{123} = \boldsymbol{D}_w : \hat{\boldsymbol{\sigma}}_{123} \quad , \tag{37}$$

where $\hat{\boldsymbol{\sigma}}_{123}$ is a non-physical stress vector, introduced for computational expediency [16,21,27,28], which is based on the product of a stiffness matrix with Poisson degradation only, $\hat{\boldsymbol{C}}$, and the strain, $\boldsymbol{\varepsilon}_{123}$. $\boldsymbol{D}_w$ is a damage tensor for woven composite ply, in which fibre and matrix damage parameters [34], $d_{11/22}$ and d_i $(\mathrm{i} = 1, 2, 3)$, are derived from a constitutive bilinear law:

$$\boldsymbol{D}_w = \begin{bmatrix} (1-d_{11}) & 0 & 0 & 0 & 0 & 0 \\ 0 & (1-d_{22}) & 0 & 0 & 0 & 0 \\ 0 & 0 & (1-d_3) & 0 & 0 & 0 \\ 0 & 0 & 0 & (1-d_1)(1-d_2) & 0 & 0 \\ 0 & 0 & 0 & 0 & (1-d_1)(1-d_3) & 0 \\ 0 & 0 & 0 & 0 & 0 & (1-d_2)(1-d_3) \end{bmatrix} . \tag{38}$$

The full expression of degraded stresses, $\sigma_{ij}(i, j = 1, 2, 3)$, is given by:

$$\sigma_{11} = (1-d_{11})\hat{\sigma}_{11} \quad , \tag{39}$$

$$\sigma_{22} = (1-d_{22})\hat{\sigma}_{22} \quad , \tag{40}$$

$$\sigma_{33} = (1-d_3)\hat{\sigma}_{33} \quad , \tag{41}$$

$$\sigma_{12} = (1-d_1)(1-d_2)\hat{\sigma}_{12} \quad , \tag{42}$$

$$\sigma_{13} = (1-d_1)(1-d_3)\hat{\sigma}_{13} \quad , \tag{43}$$

$$\sigma_{23} = (1-d_2)(1-d_3)\hat{\sigma}_{23} \quad , \tag{44}$$

where:

$$d_{11} = \begin{cases} d_{11}^C & \varepsilon_{11} < 0 \\ d_{11}^T & \varepsilon_{11} \geq 0 \; and \; d_{11}^T > d_{11}^C \\ d_{11}^C & \varepsilon_{11} \geq 0 \; and \; d_{11}^T < d_{11}^C \end{cases} ,$$

$$d_{22} = \begin{cases} d_{22}^C & \varepsilon_{22} < 0 \\ d_{22}^T & \varepsilon_{22} \geq 0 \; and \; d_{22}^T > d_{22}^C \\ d_{22}^C & \varepsilon_{22} \geq 0 \; and \; d_{22}^T < d_{22}^C \end{cases} .$$

3. Experimental evaluations

3.1 Materials and specimens

In this research, the AS4/ Polyether-ether-ketone (PEEK) woven pre-pregs were used to manufacture the woven fabric reinforced composite panels, from which the open-hole specimens were produced. All panels were subsequently inspected using a C-scan system to determine that the pristine specimens were free of any major defects. The geometry of the open-hole samples for CLC tests is shown in Fig. 3a and the pinned open-hole samples is shown in Fig. 3b, where the blue cylinder represents the steel pin, with a radius of r, used in the pinned open-hole samples. The dimensions, l_s and l_g are the fixture supported length and gauge length, respectively, L is the total length of the open-hole sample and R is the radius of the open-hole. The dimensions, w and t, are the sample width and thickness, respectively. The loading direction was defined as 0° direction. The sample dimensions are presented in Table 1.

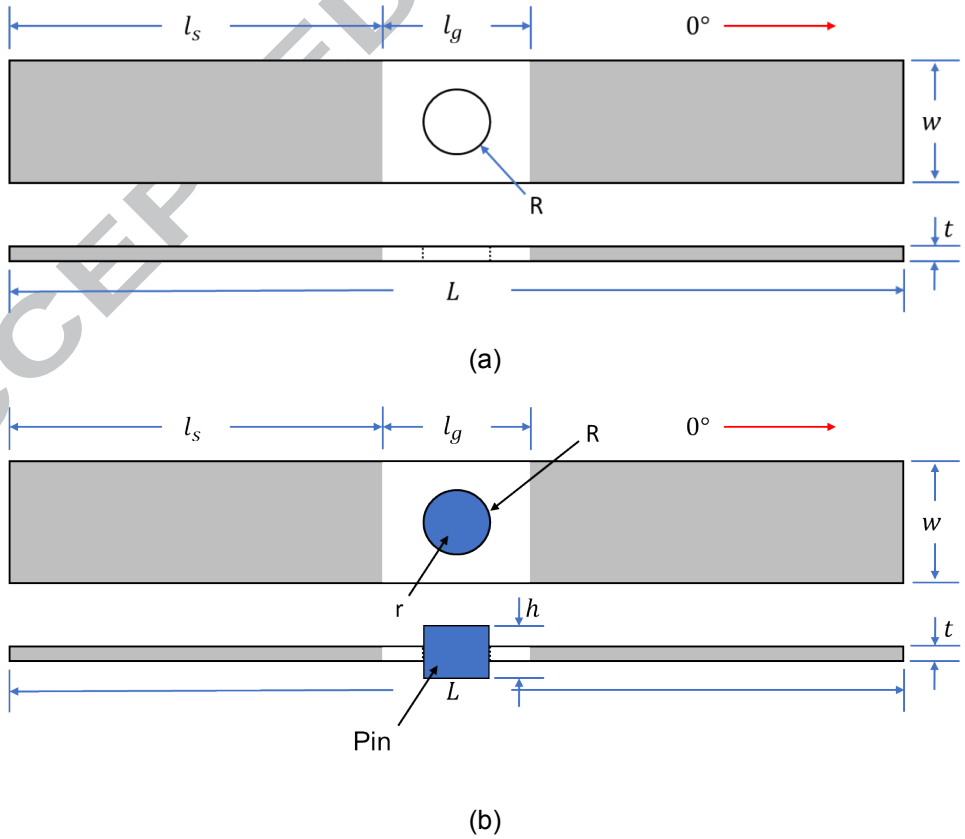

Fig. 3. CLC Specimen geometries: (a) open-hole sample and (b) pinned open-hole sample.

Table 1

Nominal dimensions of the open-hole samples for CLC tests. (mm)

Dimensions	L	l_s	l_g	R	w	t	r	h
Open-hole sample	148	64	20	5	20	1.4	N/A	N/A
Pinned open-hole sample	148	64	20	5	20	1.4	≈ 5	4

3.2 Testing methods

The CLC testing method described in ASTM standard D6641/D6641M [35] was adopted to conduct the physical tests for investigating the damage mechanisms of open-hole composite structures under compressive loading. In the CLC test, a specimen support with guide rails, Fig. 4, was used to exert the compressive load and fix the specimen.

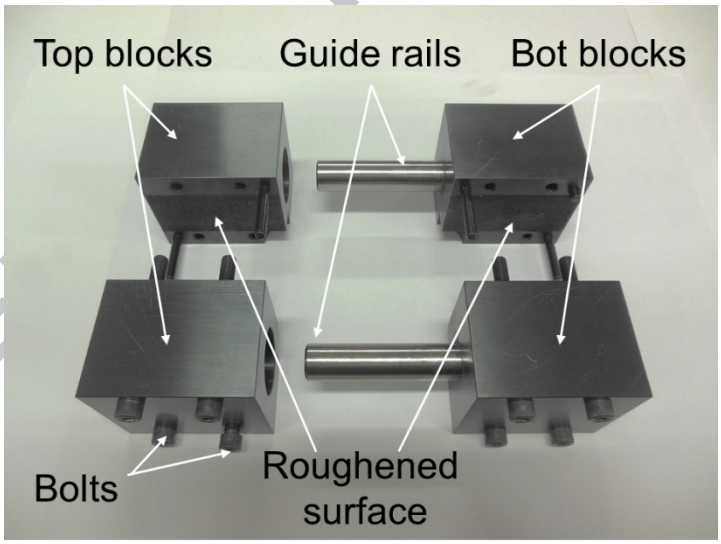

Fig. 4. Photograph of the specimen support for CLC tests.

In this research, both open-hole samples with and without a pin were tested in an *Instron*® screw-driven tensile testing machine with a 10 kN loading cell. The fixed specimen was positioned between a compression plate and a steel platform [36] shown as Fig. 5b. For both open-hole and pinned open-hole testing, three repeat samples were tested using displacement control, which was applied at a speed of 0.5 mm/s under standard laboratory temperature and environment. The pin is a close fit to

the open-hole and only held by the hole diameter. The schematic and photograph of the experimental set-up for CLC tests are shown in Figs. 5a and 5b, respectively.

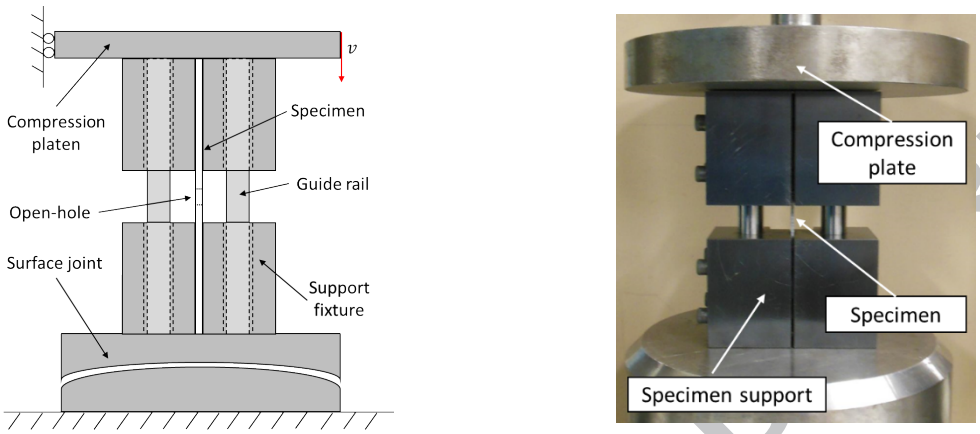

(a) (b)

Fig. 5. CLC evaluations: (a) schematic and (b) photograph of the experimental set-up.

4. Numerical simulation

4.1 Finite element model

A Computer Added Design (CAD) model, which illustrates the virtual testing set-up, is shown in Fig. 6a. The developed composite damage model was implemented as a User-defined mechanical material behaviour (VUMAT) subroutine for Abaqus/Explicit. Finite Element (FE) models of the standard open-hole sample and pinned open-hole sample were built up in Abaqus 2017 for carrying out the virtual CLC tests, Fig. 6b. The free part of the virtual open-hole structure was meshed using the eight nodes linear reduced integration (C3D8R) solid elements with a size of 0.5 mm × 0.5 mm.

The compression plate and specimen support were set as rigid bodies. The total number of elements in this finite element model was 38,280. The general contact algorithm with a friction coefficient of 0.2 was used to govern the global contact. The interfacial contact was defined as cohesive surface with a friction coefficient of 0.25 [17,20,23,37]. The computational loading speed was set as 0.5 m/s to reduce the computing time and a smooth step was used to ensure the quality of simulation was not

affected by the inertial effects. Computations were completed using 32 CPUs on a Windows Cluster with a run time of 15 h for the standard open-hole sample and 17 h for the pinned open-hole sample.

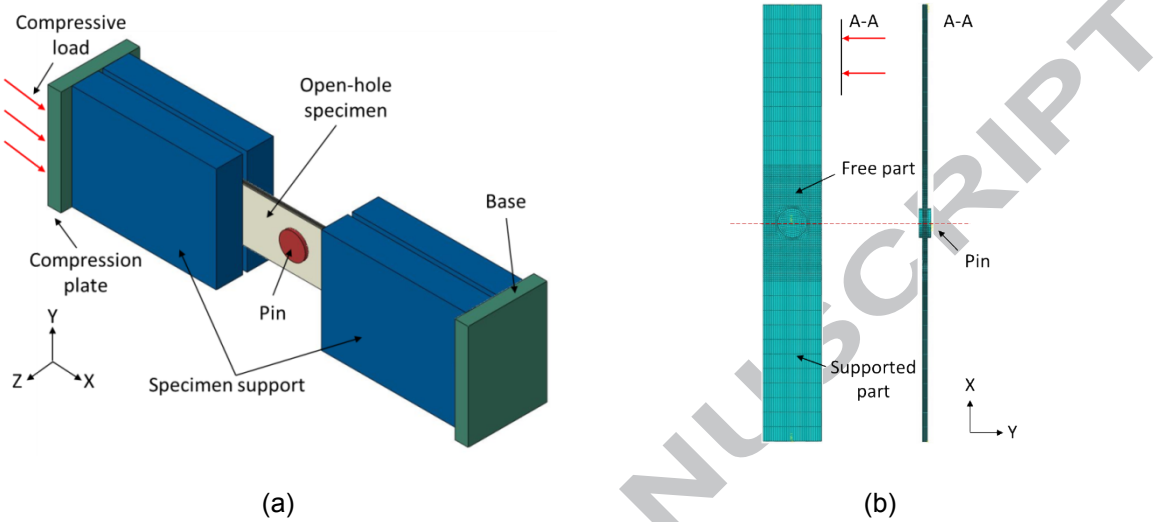

(a) (b)

Fig. 6. Virtual CLC test: (a) loading configuration and (b) FE model of pinned open-hole specimen.

4.2 Material properties

The basic material properties, such as moduli, strengths and Poisson`s ratios, required for data reduction were measured using the standard testing methods described in References [38–40]. The input parameters, such as toughness and nonlinear properties, required for the computational model were extracted from a series of material characterisation tests reported in References [32,41–46]. In details, the intralaminar fracture energies associated with fibre-dominated tensile ($G_{Ic}|_{ft}$) and compressive ($G_{Ic}|_{fc}$) failure were measured using Modified Compact Tension (MCT) and Compact Compression (CC) testing methods [30,47,48], respectively. The standard V-notched Rail Shear (VRS) testing method was used to obtain the nonlinear shear response of composite laminates [49]. The interlaminar fracture energies (G_{Ic} and G_{IIc}), and Benzeggagh–Kenane (B-K) exponent (η) were determined using standard Double-Cantilever-Beam (DCB), Four-point End-Notched-Flexure (4ENF) and Mixed-Mode-Beam (MMB) tests respectively. The material properties are shown in Table 2.

Table 2

Material properties of AS4/PEEK woven composite ply [7,50–52].

Properties	Values
Modulus (GPa)	$E_{11} = E_{22} = 63.8\ GPa$; $E_{33} = 10.3\ GPa$; $G_{13} = G_{23} = 5.0\ GPa$; $G_{12} = 5.7\ GPa$;
Poisson`s ratio	$\nu_{13} = \nu_{23} = 0.3$; $\nu_{12} = 0.05$;
Strength (MPa)	$X^T = Y^T = 801\ MPa$; $X^C = Y^C = 781\ MPa$; $Z^T = 86\ MPa$; $Z^C = 254\ MPa$; $S_{12} = 186\ MPa$;
Ply fracture toughness	$G_{Ic}\|_{ft} = 109\ kJ/\mathrm{m}^2$; $G_{Ic}\|_{fc} = 52\ kJ/\mathrm{m}^2$; $G_{Ic}\|_{mt} = 1.7\ kJ/\mathrm{m}^2$; $G_{Ic}\|_{mc} = 2.0$; $G_{IIc}\|_{ms} = 2.0\ kJ/\mathrm{m}^2$;
Shear coefficients	$c_1 = 78.4$; $c_2 = 1.88$; $c_3 = 65.7$;
Interface properties	$G_{Ic} = 1.7\ kJ/\mathrm{m}^2$; $G_{IIc} = 2.0\ kJ/\mathrm{m}^2$; $\eta = 1.09$; $\sigma_I = 43\ MPa$; $\sigma_{II} = 50\ MPa$; $k = 6.4 \times 10^5\ N/mm$;

5. Model validation

5.1 Standard open-hole samples

The experimental and numerical load versus global displacement (S) curves, obtained from standard open-hole samples, are shown in Fig. 7a. The global displacement (S), over the gauge length (l_g), has been corrected for the compliance of the testing machine and rig. Prior to peak load, the simulated load response followed the linear increase, which was also observed from experimental results. Beyond maximum load, a sudden drop, due to rupture failure, was observed from the load versus displacement curves obtained from standard open-hole samples. The comparison of load against displacement curves between experiments and simulation show that the response of the standard open-hole samples was accurately captured using the developed computational model. The computational maximum load is 4.2 kN, which is lower (-7.2%) than that present by experimental results (4.5 ± 3% kN). The total energy, which equals the area under the load-global displacement (S) curve, obtained from virtual and experimental standard open-hole samples are 227 mJ and 233 ± 5.7% mJ, respectively. In order to highlight the marginal difference, the comparison of normalised maximum load and total energy is shown in Fig. 7b, which shows good correlation between experimental and numerical results.

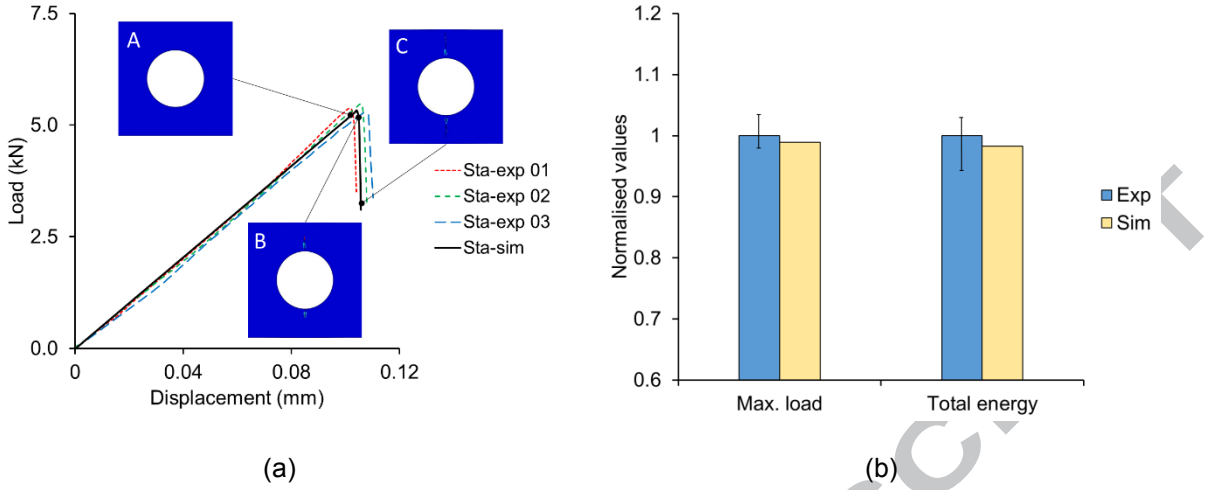

(a) (b)

Fig. 7. CLC standard open-hole experiments (Sta-exp 01 to 03) and virtual standard open-hole simulation (Sta-sim): (a) load against global displacement (S) over the gauge length (l_g) (with inset Pictures A, B and C from Fig. 8 showing simulation of the damage evolution) and (b) normalized values of maximum load and total energy.

Fig. 8 shows the damage evolution in the virtual standard open-hole sample simulation for global displacement (S) during the stages of failure. The simulation results, show that, from initial damage to final damage, the global displacement (S) only increased 0.003 mm, which means the fracture process is very short and intensive. This is also proved by the sudden drop in the load-displacement curves. The failed virtual standard open-hole sample was compared with a failed experimental standard open-hole sample in Fig. 9. In the experimental standard sample, damage due to compressive loading was observed as cracking through the ligaments between the open hole and the long edges. The comparison shows that the cracks through the whole ligament were accurately captured by the computational model.

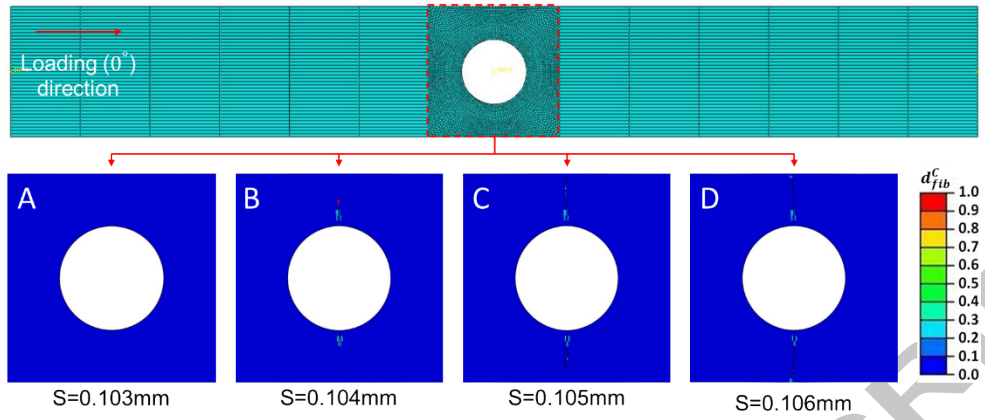

Fig. 8. Damage evolution simulation of virtual standard open-hole sample (see Fig. 7).

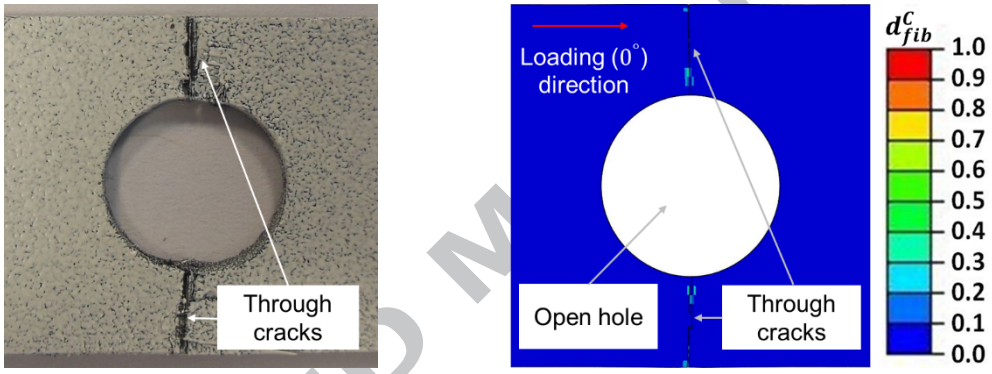

(a) (b)

Fig. 9 Failure: (a) experimental and (b) virtual standard open-hole.

5.2 Pinned open-hole samples

Fig. 10a shows load versus global displacement (S) curves, obtained from experiments and simulation of the pinned open-hole samples. It can be found that, the loading curves of pinned open-hole samples linearly increased to the maximum point, which was followed by a sudden drop. The difference between loading responses presented by standard and pinned samples is that the former presented a single drop in load, whilst, the latter presented a second growth and drop after the first drop in load. The first drop in load, for the pinned open-hole samples, was caused by an initial compressive failure about the pin leading to cracks which subsequently arrested (Picture B in Fig. 11). Following this, the pin took the load and resisted further crack growth along the middle section. The load recovered and reached a second peak load, followed by a second load drop caused by further

crack propagation across the middle section (Picture C in Fig. 12a). This discontinuous crack propagation procedure in the pinned open-hole samples was due to the steel pin, which constrained the deformation around the open-hole region. Also, the pinned samples withstood a higher peak load (5.97 ± 2.4% kN) than the standard open-hole samples (4.5 ± 3% kN). The maximum loads obtained from physical and virtual pinned open-hole samples are 5.97 ± 2.4% kN and 5.93 kN, respectively.

The computational total energy (271 mJ) is marginally lower (-3%) than the experimental values (279 ± 2.1% mJ). Fig. 10b shows the comparison of normalised maximum load and total energy obtained from physical and virtual pinned open-hole samples, which demonstrates a good agreement between experimental and numerical results. To be noted is that, with a steel pin, greater load is carried by the structure and the global displacement (S) is reduced, however, overall the total energy is increased for the pinned open-hole.

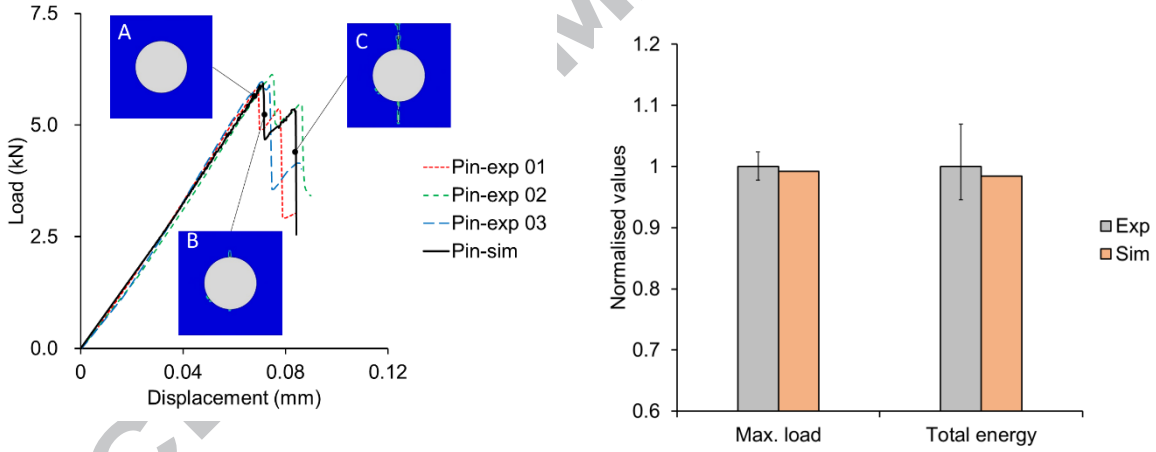

(a) (b)

Fig. 10. CLC pinned open-hole experiments (Pin-exp 01 to 03) and virtual pinned open-hole simulation (Pin-sim): (a) load against global displacement (S) over the gauge length (l_g) (with inset Pictures A, B and C from Fig. 11 showing simulation of the damage evolution) and (b) normalized values of maximum load and total energy.

The damage evolution obtained from virtual pinned open-hole sample simulation is shown in Fig 11 for global displacement (S) during the stages of failure. The failed experimental and virtual pinned open-hole samples are compared in Fig. 12. As for the standard open-hole samples, through-

thickness cracks were observed in the ligament regions of both experimental and virtual pinned open-hole samples. The difference is the compressive failure was observed in the image obtained from the experimental pinned open-hole specimens (Fig. 12a), and the compressive failure was also well reproduced by the computational model, Fig. 12b, which confirmed the capability of the proposed composite damage model in capturing the response of woven fabric reinforced composite laminates.

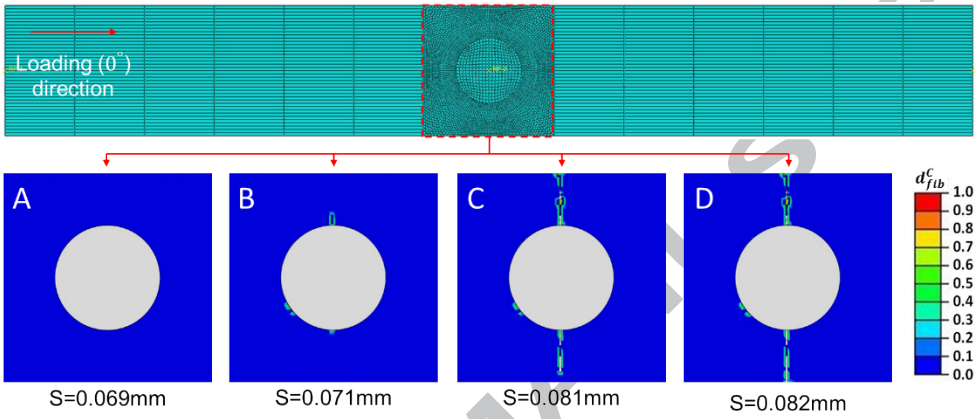

Fig. 11. Damage evolution simulation of virtual pinned open-hole sample (see Fig. 10).

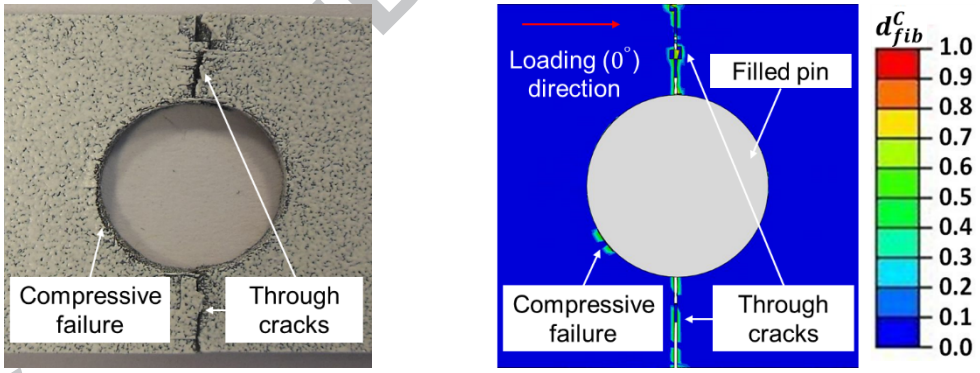

(a) (b)

Fig. 12. Failure: (a) experimental and (b) virtual pinned open-hole samples.

6. Conclusions

In this research, two types of composite samples, the standard open-hole and the pinned open-hole samples, were evaluated using the Combined Loading Compression (CLC) test method, described in ASTM 6641, to investigate the damage mechanisms of open-hole and pinned open-hole woven fabric

reinforced thermoplastic composite laminates under compressive loading. The corresponding virtual compression test was simulated using a computational model, which was developed for Abaqus/Explicit. The capability of the computational model in capturing the response of woven composite laminates under compressive loading was validated using the extracted experimental results. A good correlation was achieved between experimental and numerical results.

From these experiments and simulations, it was found that a single load peak, and subsequent crack propagation across the ligament, was observed in the open-hole samples. By comparison, the pinned open-hole samples exhibited two load peaks and a two-stage crack propagation with greater load carrying capability and greater total energy absorbed before failure. This is due to the presence of the steel pin, which constrained the material deformation around the open-hole. The importance and benefit of a pin (or bolt) is demonstrated. The simulations captured these effects well and the research has shown that the meso-scale damage modelling approach, based on Continuum-Damage-Mechanics (CDM), can very effectively simulate the onset of damage and subsequent crack propagation in woven fabric reinforced composites. This is for open-hole and pinned open-hole configurations, which are often present, when composite materials are fixed (or bolted) together in aircraft structures.

Acknowledgements

The authors are grateful to the Aviation Industry Corporation of China (AVIC), the First Aircraft Institute (FAI) and the Manufacturing Technology Institute (MTI) through the AVIC Centre for Structural Design and Manufacture (SDM) at Imperial College London, for supporting Drs Haibao Liu, Jun Liu and Hui Chai. The strong support from the Research Computing Team (RCT) at Imperial College London, in providing access to the High-Performance Computing (HPC) facilities, was very helpful. The authors also much appreciate the use of experimental facilities at Tianjin University, People's Republic of China.

References

[1] Goyal VK, Jaunky NR, Johnson ER, Ambur DR. Intralaminar and interlaminar progressive failure analyses of composite panels with circular cutouts. Compos Struct, 2004;64:91–105.

[2] O'Higgins RM, McCarthy M a., McCarthy CT. Comparison of open hole tension characteristics of high strength glass and carbon fibre-reinforced composite materials. Compos Sci Technol, 2008;68:2770–8.

[3] Ansari M, Chakrabarti A. Impact behavior of FRP composite plate under low to hyper velocity impact. Compos Part B Eng, 2016;95:462–74.

[4] Budiansky B, Fleck NA. Compressive failure of fibre composites. J Mech Phys Solids, 1993;41:183–211.

[5] Jia L, Yu L, Zhang K, Li M, Jia Y, Blackman BRK, et al. Combined modelling and experimental studies of failure in thick laminates under out-of-plane shear. Compos Part B Eng, 2016;105:8–22.

[6] Bouvet C, Rivallant S, Barrau JJ. Low velocity impact modeling in composite laminates capturing permanent indentation. Compos Sci Technol, 2012;72:1977–88.

[7] Tan W, Falzon BG. Modelling the nonlinear behaviour and fracture process of AS4/PEKK thermoplastic composite under shear loading. Compos Sci Technol, 2016;126:60–77.

[8] Setoodeh AR, Malekzadeh P, Nikbin K. Low velocity impact analysis of laminated composite plates using a 3D elasticity based layerwise FEM. Mater Des, 2009;30:3795–801.

[9] Chiu LNS, Falzon BG, Boman R, Chen B, Yan W. Finite element modelling of composite structures under crushing load. Compos Struct, 2015;131:215–28.

[10] Suiker ASJ, Fleck NA. Modelling of fatigue crack tunneling and delamination in layered composites. Compos Part A Appl Sci Manuf, 2006;37:1722–33.

[11] Zhang Y, Zhu P, Lai X. Finite element analysis of low-velocity impact damage in composite laminated plates. Mater Des, 2006;27:513–9.

[12] Tan W, Falzon BG. Modelling the crush behaviour of thermoplastic composites. Compos Sci Technol, 2016;134:57–71.

[13] Parsons EM, Weerasooriya T, Sarva S, Socrate S. Impact of woven fabric: Experiments and mesostructure-based continuum-level simulations. J Mech Phys Solids, 2010;58:1995–2021.

[14] Iannucci L, Willows ML. An energy based damage mechanics approach to modelling impact onto woven composite materials — Part I : Numerical models. Compos Part A Appl Sci Manuf, 2006;37:2041–56.

[15] L.Iannucci, M.L.Willows. An energy based damage mechanics approach to modelling impact onto woven composite materials: Part II. Experimental and numerical results. Compos Part A Appl Sci Manuf, 2007;38:540–54.

[16] Donadon MV, Falzon BG, Iannucci L, Hodgkinson JM. A 3-D micromechanical model for predicting the elastic behaviour of woven laminates. Compos Sci Technol, 2007;67:2467–77.

[17] Liu H, Falzon BG, Tan W. Experimental and numerical studies on the impact response of damage-tolerant hybrid unidirectional/woven carbon-fibre reinforced composite laminates. Compos Part B Eng, 2018;136:101–18.

[18] Donadon MV, Iannucci L, Falzon BG, Hodgkinson JM, de Almeida SFM. A progressive failure model for composite laminates subjected to low velocity impact damage. Comput Struct, 2008;86:1232–52.

[19] Faggiani A, Falzon BG. Predicting low-velocity impact damage on a stiffened composite panel. Compos Part A Appl Sci Manuf, 2010;41:737–49.

[20] Chiu LNS, Falzon BG, Chen B, Yan W. Validation of a 3D damage model for predicting the response of composite structures under crushing loads. Compos Struct, 2016;147:65–73.

[21] Falzon BG, Liu H, Tan W. Comment on A tensorial based progressive damage model for fiber reinforced polymers. Compos Struct, 2017;176:877–82.

[22] Tan W, Falzon BG, Chiu LNS, Price M. Predicting low velocity impact damage and Compression-After-Impact (CAI) behaviour of composite laminates. Compos Part A Appl Sci Manuf, 2015;71:212–26.

[23] Liu H, Falzon BG, Tan W. Predicting the Compression-After-Impact (CAI) strength of damage-tolerant hybrid unidirectional/woven carbon-fibre reinforced composite laminates. Compos Part A Appl Sci Manuf, 2017;105:189–202.

[24] Daniel IM, Luo JJ, Schubel PM. Three-dimensional characterization of textile composites. Compos Part B Eng, 2008;39:13–9.

[25] Chaboche, J.L. Continuum Damage Mehcanics: Part I---General Concepts. J Appl Mech, 1988;55:59–64.

[26] Lemaitre J, Chaboche JL. Mechanics of solid materials. Cambridge: Cambridge University Press; 1990.

[27] Falzon BG, Apruzzese P. Numerical analysis of intralaminar failure mechanisms in composite structures. Part I FE implementation. Compos Struct, 2011;93:1039–46.

[28] Falzon BG, Apruzzese P. Numerical analysis of intralaminar failure mechanisms in composite structures. Part II: Applications. Compos Struct, 2011;93:1047–53.

[29] Davila CG, Camanho PP, Rose CA. Failure Criteria for FRP Laminates. J Compos Mater, 2005;39:323–45.
[30] Tan W, Falzon BG, Price M, Liu H. The role of material characterisation in the crush modelling of thermoplastic composite structures. Compos Struct, 2016;153:914–27.
[31] Benzeggagh ML, Kenane M. Measurement of mixed-mode delamination fracture toughness of unidirectional glass/epoxy composites with mixed-mode bending apparatus. Compos Sci Technol, 1996;56:439–49.
[32] ASTM. Standard Test Method for Mixed Mode I-Mode II Interlaminar Fracture Toughness of Unidirectional Fiber Reinforced Polymer Matrix Composites, D6671/D 6671M-03, West Conshohocken, PA. 2003.
[33] Abaqus 6.12 documentation. Dassault Systèmes. Provid Rhode Island, USA, 2012.
[34] Donadon MV, Falzon BG, Iannucci L, Hodgkinson JM. Intralaminar toughness characterisation of unbalanced hybrid plain weave laminates. Compos Part A Appl Sci Manuf, 2007;38:1597–611.
[35] ASTM. Standard Test Method for Compressive Properties of Polymer Matrix Composite Materials Using a Combined Loading Compression (CLC) Test Fixture, D6641 / D6641M, West Conshohocken, PA. 2009.
[36] Catalanotti G, Arteiro A, Hayati M, Camanho PP. Determination of the mode I crack resistance curve of polymer composites using the size-effect law. Eng Fract Mech, 2014;118:49–65.
[37] Rolfe E, Quinn R, Sancho A, Kaboglu C, Johnson A, Liu H, et al. Blast resilience of composite sandwich panels with hybrid glass-fibre and carbon-fibre skins. Multiscale Multidiscip Model Exp Des, 2018;1:197–210.
[38] ASTM. Standard Test Method for Young's Modulus, Tangent Modulus, and Chord Modulus. E111 - 04, West Conshohocken, PA, 2004.
[39] ASTM. Standard Test Method for Poisson's Ratio at Room Temperature. E132 - 04, West Conshohocken, PA, 2004.
[40] ASTM. Standard Test Method for Tensile Properties of Polymer Matrix Composite Materials. D3039/D3039M - 14, West Conshohocken, PA, 2014.
[41] ASTM. Standard Test Method for Determination of the Mode II Interlaminar Fracture Toughness of Unidirectional Fiber-Reinforced Polymer Matrix Composites, D7905/D7905M-14, West Conshohocken, PA. 2014.
[42] ASTM. Standard Test Method for Mode I Interlaminar Fracture Toughness of Unidirectional Fiber-Reinforced Polymer Matrix Composites, D5528-01, West Conshohocken, PA. 2004.
[43] Pinho ST, Robinson P, Iannucci L. Fracture toughness of the tensile and compressive fibre failure modes in laminated composites. Compos Sci Technol, 2006;66:2069–79.
[44] ASTM. Standard Test Method for Shear Properties of Composite Materials by V-Notched Rail Shear Method, D7078/D7078M-05, West Conshohocken, PA. 2005.
[45] Schuecker C, Davidson BD. Evaluation of the accuracy of the four-point bend end-notched flexure test for mode II delamination toughness determination. Compos Sci Technol, 2000;60:2137–46.
[46] Liu H, Falzon BG, Catalanotti G, Tan W. An experimental method to determine the intralaminar fracture toughness of high-strength carbon-fibre reinforced composite aerostructures. Aeronaut J, 2018;122:1352–70.
[47] Catalanotti G, Camanho PP, Xavier J, Dávila CG, Marques AT. Measurement of resistance curves in the longitudinal failure of composites using digital image correlation. Compos Sci Technol, 2010;70:1986–93.
[48] Camanho PP, Catalanotti G. On the relation between the mode I fracture toughness of a composite laminate and that of a 0 ply: Analytical model and experimental validation. Eng Fract Mech, 2011;78:2535–46.
[49] Catalanotti G, Xavier J. Measurement of the mode II intralaminar fracture toughness and R-curve of polymer composites using a modified Iosipescu specimen and the size effect law. Eng Fract Mech, 2015;138:202–14.
[50] MIL HDBK-17-2F. Composite Materials Handbook. Def Stand Progr Off, 2002;2–5:689.
[51] CYTEC. APC-2-PEEK Thermoplastic Polymer. Https://WwwCytecCom/Sites/Default/Files/Datasheets/APC-2_PEEK_031912-01Pdf, 2012.
[52] Naderi M, Khonsari MM. Stochastic analysis of inter- and intra-laminar damage in notched PEEK laminates. Express Polym Lett, 2013;7:383–95.